

Rethinking the Ozone-Climate Change Penalty

Xiyue Zhang¹, Darryn W Waugh¹, Gaige Hunter Kerr², and Scot M Miller^{1,3}

¹Department of Earth and Planetary Sciences, Johns Hopkins University, Baltimore, Maryland, USA

²Department of Environmental and Occupational Health, Milken School of Public Health, George

Washington University, Washington, DC, USA

³Department of Environmental Health and Engineering, Johns Hopkins University, Baltimore, Maryland,

USA

Key Points:

- Transport by meridional advection of O_3 and T explains the spatial variations in daily O_3 - T relationship
- Daily regression slope dO_3/dT can be estimated by the ratio of O_3 and T mean meridional gradients when temperature gradients are strong
- Gradient ratio suggests dO_3/dT to change with warming, making it questionable to use observed dO_3/dT in O_3 projection

Corresponding author: Xiyue Zhang, sallyz@jhu.edu

Abstract

The daily variation of ground-level ozone (O_3), a harmful pollutant, is positively correlated with air temperature (T) in many midlatitude land regions in the summer. The observed temporal regression slope between O_3 and T is referred to as the “ozone-climate change penalty” and has been proposed as a way to predict the impact of future climate warming on O_3 from observations. Here, we use two chemical transport models to show that the O_3 - T correlation is primarily due to the meridional advection of both fields, as opposed to direct temperature-dependent chemistry or emissions. Furthermore, the magnitude of the O_3 - T regression (dO_3/dT) can be estimated by the ratio of the time-mean O_3 and T meridional gradients. Consideration of expected changes in the meridional gradients of T and O_3 due to climate change indicates that dO_3/dT will likely change, and caution is needed when using the observed climate penalty to predict O_3 changes.

Plain Language Summary

At Earth’s surface, ozone is a harmful pollutant. In the summer, we observe higher ozone concentrations on hotter days in many land regions in the midlatitudes. This leads researchers to expect higher ozone concentrations as a result of global warming, based on chemistry that associates higher ozone concentrations with higher temperatures. Here, we show that the relationship between ozone and temperature is largely controlled by atmospheric transport. In particular, north-south movement of air transports both ozone and heat simultaneously. Therefore, the background spatial distributions of ozone and temperature determine how ozone and temperature covary from day to day. The ozone-temperature relationship in the future may look different from today, because global warming is not spatially uniform. We advise caution in using observed ozone-temperature relationship to estimate future ozone changes.

1 Introduction

Ground-level ozone (O_3) is a pollutant harmful to human health and ecosystem productivity (Landrigan et al., 2018; Tai & Val Martin, 2017; Wittig et al., 2007). Observations show that summer O_3 concentrations tend to be higher when temperatures are warmer (e.g., Bloomer et al., 2009; Kerr & Waugh, 2018; Schnell & Prather, 2017). This empirical relationship raises the possibility that a warmer climate would lead to higher O_3 concentrations, which would then require additional emission controls to meet a given

46 O₃ target (Wu et al., 2008). This increase in O₃ with temperature is referred to as the
 47 “ozone-climate change penalty” (or “ozone climate penalty”), and there has been exten-
 48 sive research into the magnitude of this penalty (see Rasmussen et al. (2013) and Fu and
 49 Tian (2019) for reviews). A common metric for the ozone climate penalty is the slope
 50 of the ozone-temperature (O₃-*T*) relationship dO_3/dT (Bloomer et al., 2009), which can
 51 be calculated from observations and models. It has been proposed that this metric could
 52 be used to predict the impact of future climate warming on ozone. A similar “climate
 53 penalty” for fine particulate matter (PM_{2.5}) also suggests an increase of PM_{2.5} in a warmer
 54 climate (Westervelt et al., 2016; Shen et al., 2017).

55 However, the use of a climate penalty to predict changes in a future climate requires
 56 the assumption that dO_3/dT (or $dPM_{2.5}/dT$) does not change with climate. Whether
 57 dO_3/dT is invariant to climate change will depend on the cause of the O₃-*T* relationship.
 58 If the relationship is due to the direct and close to linear temperature dependence of chem-
 59 ical reactions or ozone precursor emissions, it is likely dO_3/dT will not change with cli-
 60 mate. However, if the relationship is caused by an indirect association between O₃ and
 61 *T*, then the relationship may change under a changing climate. Recent studies indicate
 62 that the majority of the O₃-*T* relationship is explained by their indirect association due
 63 to atmospheric transport (e.g., Porter & Heald, 2019; Kerr et al., 2019, 2020), suggest-
 64 ing dO_3/dT will change with the climate. Here, we revisit the processes controlling dO_3/dT ,
 65 extending the recent studies of Kerr et al. (2020) and Kerr et al. (2021). These studies
 66 showed that the O₃-*T* relationship within midlatitudes is primarily due to jet-induced
 67 changes in the surface-level meridional advection of O₃, and spatial variation of the sign
 68 of the relationship can be related to changes in the sign of the meridional gradients. We
 69 hypothesize that the importance of the surface-level meridional advection holds globally
 70 and also applies to temperature, so that dO_3/dT can be estimated by the ratio of the
 71 meridional ozone and temperature gradients.

72 On the planetary scale, the meridional gradients of scalars such as temperature,
 73 specific humidity, and O₃ dominate their zonal gradients. If meridional advection plays
 74 the leading role in shaping the large-scale distribution and variability of these scalars,
 75 then the tendencies of any two arbitrary scalars x_1 and x_2 are $\partial_t x_1 \approx v \partial_\phi x_1$ and $\partial_t x_2 \approx$
 76 $v \partial_\phi x_2$ (∂_t is partial derivative with respect to time, v is meridional velocity, and ϕ is lat-

77 itude). This implies

$$\frac{dx_1}{dx_2} \approx \frac{\partial_\phi x_1}{\partial_\phi x_2}, \quad (1)$$

78 i.e., the relationship between two scalars dx_1/dx_2 can be approximated by the ratio of
 79 the x_1 meridional gradients to the x_2 meridional gradients (referred to as the “gradient
 80 ratio” below). For the case of O_3 and T this then becomes

$$\frac{dO_3}{dT} \approx \frac{\partial_\phi O_3}{\partial_\phi T}. \quad (2)$$

81 In this paper, we test this hypothesis first using idealized passive tracers from Kerr et
 82 al. (2021) where chemistry is absent, and then in more realistic simulations of O_3 . We
 83 demonstrate that the spatial pattern and magnitude of dO_3/dT can be quantitatively
 84 determined by their gradient ratio $\partial_\phi O_3/\partial_\phi T$ in regions with strong meridional temper-
 85 ature gradients. Furthermore, this framework also applies to explaining the O_3 and spe-
 86 cific humidity relationship, as well as the relationship between two chemical tracers with
 87 different source regions. We introduce the data sets and methods used in our analyses
 88 in Section 2. Next, we test our hypothesis using idealized passive tracer experiments in
 89 Section 3, followed by analysis of the ozone-meteorology relationship in Section 4. We
 90 then discuss the implications in Section 5 and summarize our results in Section 6.

91 2 Methods

92 2.1 GEOS-Chem Idealized Tracers

93 We analyze simulations of passive tracers with prescribed zonally symmetric emis-
 94 sions using the GEOS-Chem chemical transport model (CTM, v12.0.2) analyzed by Kerr
 95 et al. (2021). These simulations are driven by meteorological fields from the Modern Era-
 96 Retrospective Analysis for Research and Analysis, Version 2 (MERRA-2) from 2008 to
 97 2010, with a horizontal resolution of 2° latitude \times 2.5° longitude ($\sim 200 \times 250$ km) and 72
 98 vertical levels. Tracers emitted in 10° latitudinal bands have a uniform 50 days^{-1} loss
 99 rate. Tracer mixing ratios are denoted $\chi_{\phi_1-\phi_2}$, where ϕ_1 and ϕ_2 are the latitudes of south-
 100 ern and northern emission boundaries. We focus on χ_{40-50} (tracer emitted between 40° -
 101 50° N) here to represent midlatitude emissions. We also discuss χ_{20-30} and χ_{60-70} to rep-
 102 resent the subtropical and subpolar regions and demonstrate the robustness of our re-
 103 sults.

2.2 GMI Ozone Simulations

We also analyze O_3 from simulations of NASA’s Global Modeling Initiative chemical transport model (GMI CTM, Duncan et al., 2007; Strahan et al., 2007, 2013) analyzed in Kerr et al. (2020). These simulations are also driven by MERRA-2 fields from 2008 to 2010, with a horizontal resolution of 1° latitude \times 1.25° longitude (~ 100 km) and 72 vertical levels. Early afternoon O_3 (averaged between 1300–1400 hr local time) is analyzed to represent peak daily O_3 concentrations. GMI CTM simulations have demonstrated realistic O_3 variability and its drivers when compared to observations (Strode et al., 2015; Kerr et al., 2019, 2020).

To isolate the role of transport, we also analyze an additional GMI CTM sensitivity simulation from Kerr et al. (2020) where daily variations in natural and anthropogenic emissions and chemistry related processes (e.g., temperature, specific humidity, clouds, etc.) are fixed to monthly mean values. Daily variability in this “transport-only” simulation stems solely from variations in transport (e.g., wind, boundary layer dynamics, etc.).

2.3 Analysis Methods

We focus on the northern hemisphere domain of 10 – 70° N. The GMI output and MERRA-2 fields are interpolated onto the lower resolution of GEOS-Chem CTM, so that the analysis of the idealized tracers and O_3 is done at the same resolution. We analyze the near-surface (1000–800 hPa) tracer mixing ratios of idealized tracers and O_3 from the model’s surface level. We use 2-m daily maximum temperature (T) and 2-m daily-mean specific humidity (Q) from MERRA-2 to represent meteorology. For all fields, daily anomalies are calculated by removing the 2008–2010 monthly climatology at each grid point. Boreal summer (June, July, and August (JJA)) data consist of 276 daily anomalies (concatenating 3 years of JJA data), while boreal winter (December, January, and February (DJF)) data consist of 270 daily anomalies.

Linear least-squares regression between anomalies of tracer concentration and T (or Q) is computed with the Scipy package `linregress`. Regions with $p > 0.05$ are hatched on maps and defined as not statistically significant. Meridional gradients are calculated by differentiating fields averaged over 2008–2010 JJA (or DJF) with the second order accurate central differences along latitudes. All meridional gradients are then smoothed

135 by a 2-D convolution with a kernel of 10° latitude \times 12.5° longitude box for better vi-
 136 sualization. The gradient ratios presented are the ratios of the smoothed meridional gra-
 137 dients. Our results are not sensitive to a smaller kernel box.

138 3 Idealized Passive Tracers

139 We first consider the relationship between an idealized tracer with a 50 days^{-1} loss
 140 rate and zonally symmetric emissions at $40\text{--}50^\circ\text{N}$ (broadly the region of ozone precur-
 141 sor emissions) χ_{40-50} and T . Even though there is no direct association between χ_{40-50}
 142 and T (i.e., the tracer source and loss rate are independent of temperature), they are sig-
 143 nificantly correlated on daily timescales as shown by the JJA daily regression $d\chi_{40-50}/dT$
 144 on Figure 1a. There is a prominent spatial pattern where $d\chi_{40-50}/dT$ is positive north
 145 of the emission region ($40\text{--}50^\circ\text{N}$) and negative south of this region. The absolute val-
 146 ues are the highest over midlatitude oceans, but the regression remains significant ($p <$
 147 0.5) over land. Other zonally asymmetric features include the change in signs over main
 148 topographic features such as the northern Rockies and the Himalayas.

149 Next, we look at the meridional gradients of χ_{40-50} and T to determine whether
 150 the spatial pattern of gradient ratio $\partial_\phi\chi_{40-50}/\partial_\phi T$ agrees with $d\chi_{40-50}/dT$, as suggested
 151 by (1). As the tracer emissions are zonally symmetric, the tracer concentrations are close
 152 to being zonally symmetric and highest at the latitudes of emission (see Figure 1 of Kerr
 153 et al. (2021)). The meridional gradient of the tracer $\partial_\phi\chi_{40-50}$ is negative to the north
 154 and positive to the south of the emission region (Figure 1b contours). In contrast, the
 155 meridional temperature gradient $\partial_\phi T$ has the same sign (negative) over most of the North-
 156 ern Hemisphere, with exceptions for regions of significant topography and near the equa-
 157 tor (the peak summer T occurs in the subtropics, Figure 1b shading). As a result, the
 158 spatial pattern of their gradient ratio (Figure 1c) is largely consistent with $d\chi_{40-50}/dT$
 159 (Figure 1a), with generally positive values north of the emission region and negative val-
 160 ues south of the emissions, except near the equatorial land. However, there are differ-
 161 ences in magnitude.

162 We compute the regional average of $d\chi_{40-50}/dT$ and $\partial_\phi\chi_{40-50}/\partial_\phi T$ to quantita-
 163 tively compare both quantities and avoid extreme values of $\partial_\phi\chi_{40-50}/\partial_\phi T$ due to local
 164 weak temperature gradient (small $|\partial_\phi T|$). We focus on averaging domains of 10° lati-
 165 tude \times 20° longitude and calculate the root-mean-square error (RMSE) between the two

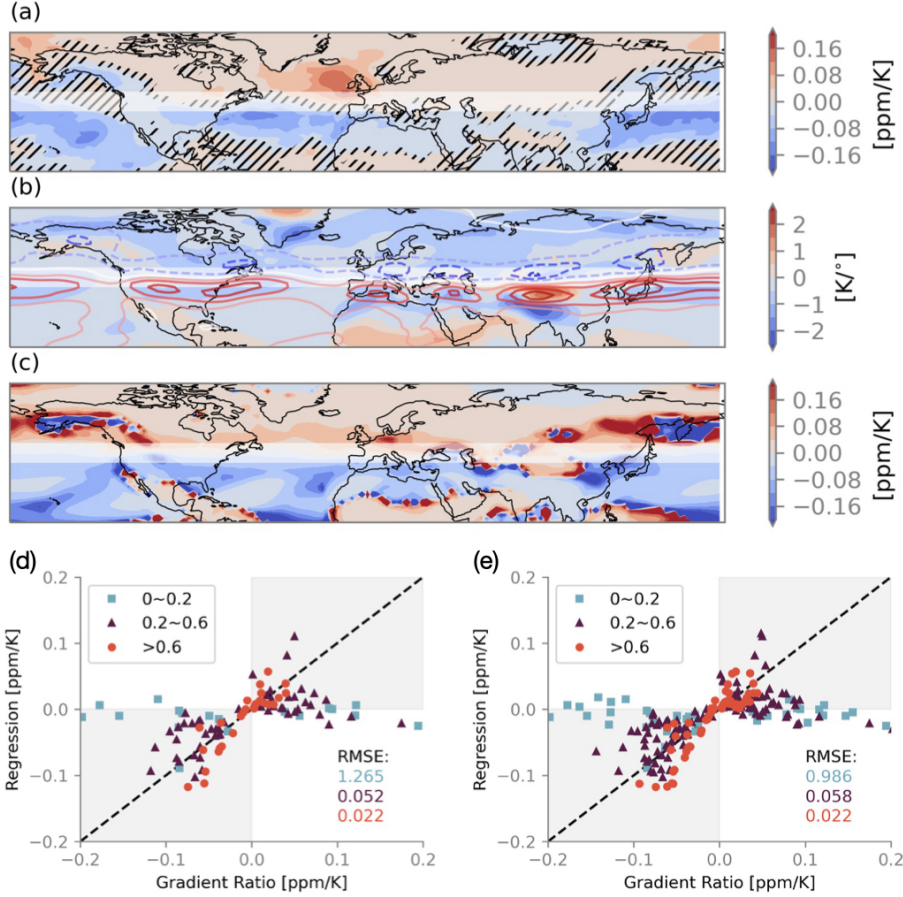


Figure 1. 2008–2010 JJA relationship between idealized tracer emitted from 40–50°N (white bands) χ_{40-50} and daily maximum 2-m temperature T . (a) Daily $d\chi_{40-50}/dT$ regression slope from GEOS-Chem simulation. Regions with $p > 0.05$ (not statistically significant) are hatched. (b) Mean meridional gradient temperature $\partial_\phi T$ in shading and of idealized tracer $\partial_\phi \chi_{40-50}$ in contours (interval of 0.02 ppm/°, positive in solid contours). (c) Gradient ratio $\partial_\phi \chi_{40-50}/\partial_\phi T$. (d) Scatter plot of gradient ratio $\partial_\phi \chi_{40-50}/\partial_\phi T$ versus regression $d\chi_{40-50}/dT$ averaged over 10° latitude × 20° longitude domains, binned by the absolute value of meridional temperature gradient $|\partial_\phi T|$ (K/° in legends). Dashed line shows the 1:1 slope. RMSE between gradient ratio and regression for each $|\partial_\phi T|$ bin is indicated. (e) Same as (d) but averaged over 10° latitude × 10° longitude domains.

166 quantities to measure the agreement. The agreement between $d\chi_{40-50}/dT$ and $\partial_\phi \chi_{40-50}/\partial_\phi T$
 167 varies with $|\partial_\phi T|$ (Figure 1d). When the meridional temperature gradient is strong ($|\partial_\phi T| >$
 168 0.6 K/°), the gradient ratio and regression are close to the 1:1 line, and the RMSE is only
 169 0.022 ppm/K (circles). Regions with $|\partial_\phi T| > 0.6$ K/° include northeastern North Amer-

170 ica, the Mediterranean, northeastern Europe, and central Pacific. In regions with mod-
 171 erate temperature gradients ($0.2 < |\partial_\phi T| < 0.6$ K/°; triangles), the approximation is
 172 less accurate (RMSE = 0.052 ppm/K), but we still find agreement between the signs of
 173 $d\chi_{40-50}/dT$ and $\partial_\phi\chi_{40-50}/\partial_\phi T$, i.e., $\partial_\phi\chi_{40-50}/\partial_\phi T$ predicts the sign of $d\chi_{40-50}/dT$. Many
 174 land regions (e.g., Europe, western North America, North Africa, northeastern Asia) have
 175 moderate meridional temperature gradients. When the temperature gradient is weaker
 176 than 0.2 K/° (squares), the regression between χ_{40-50} and T is not significant. Trop-
 177 ical oceans, South Asia, and a part of East Asia fall into this category. This weak rela-
 178 tionship is expected: when the temperature gradients are weak the meridional advec-
 179 tion of T will only play a minor role in the temperature tendency equation, and the as-
 180 sumption $\partial_t T \approx v\partial_\phi T$ used in deriving (1) is not valid.

181 To test the sensitivity to the size of the averaging domains, we average over smaller
 182 regions of 10° latitude \times 10° longitude, and the main results still hold (Figure 1e): RMSE
 183 is the largest for the weakest temperature gradients and smallest for the strongest tem-
 184 perature gradients. The same applies for even smaller domains of 5° latitude \times 5° lon-
 185 gitude.

186 A similar agreement between the daily regression $d\chi/dT$ and the gradient ratio is
 187 found for idealized tracers with different emission regions. For example, Figure 2a shows
 188 the comparison between regression and gradient ratio for an idealized tracer with emis-
 189 sions between $20-30^\circ$ N (χ_{20-30}). The meridional gradient of χ_{20-30} is negative over most
 190 of the hemisphere, which results in a generally positive $\partial_\phi\chi_{20-30}/\partial_\phi T$ consistent with
 191 the positive $d\chi_{20-30}/dT$. The RMSE between $\partial_\phi\chi_{20-30}/\partial_\phi T$ and $d\chi_{20-30}/dT$ is only 0.015
 192 ppm/K when $|\partial_\phi T| > 0.6$ (circles), but becomes 0.052 ppm/K when $0.2 < |\partial_\phi T| <$
 193 0.6 K/° (triangles). Similarly, the tracer with emissions between $60-70^\circ$ N (χ_{60-70}) gen-
 194 erally has positive $\partial_\phi\chi_{60-70}$ and negative $\partial_\phi\chi_{60-70}/\partial_\phi T$, where we find small RMSE for
 195 large $|\partial_\phi T|$ (not shown). All three idealized tracers demonstrate that gradient ratios can
 196 robustly approximate the relationship between χ and T on a daily timescale.

197 The agreement between gradient ratio and $d\chi/dT$ also holds in other seasons. In
 198 fact, $|\partial_\phi T|$ in DJF are much stronger than in JJA, and the RMSE between $d\chi_{40-50}/dT$
 199 and $\partial_\phi\chi_{40-50}/\partial_\phi T$ are lower than those in JJA for all three $|\partial_\phi T|$ bins (Figure 2b).

200 Equation (1) should hold not only for tracer-temperature relationships but also for
 201 other meteorological dependencies. One such dependency is specific humidity (Q), and

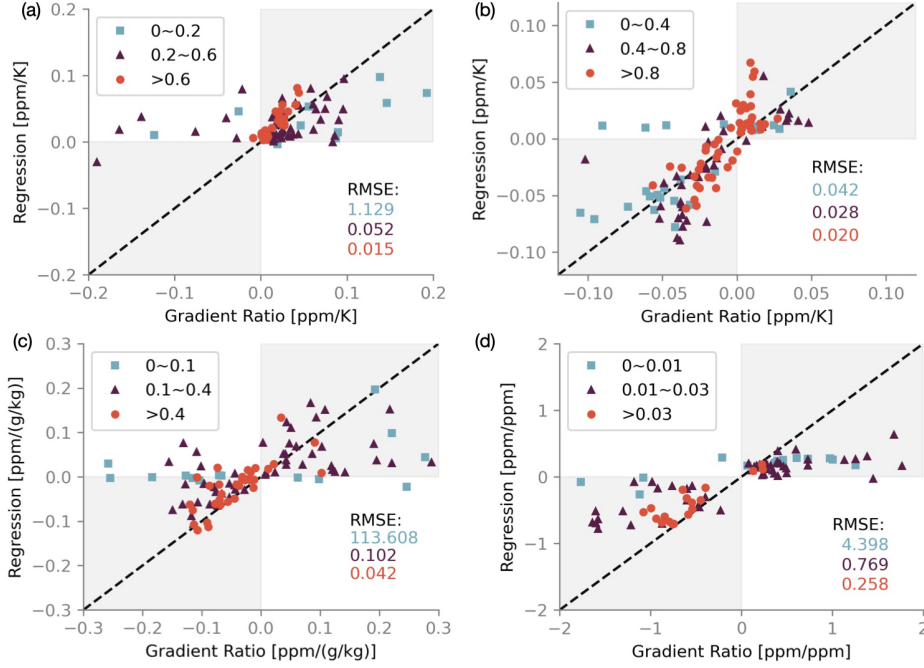


Figure 2. Idealized tracer scatter plots averaged over 10° latitude \times 20° longitude regions. (a) JJA gradient ratio $\partial_\phi \chi_{20-30} / \partial_\phi T$ versus regression $d\chi_{20-30} / dT$, binned by their absolute value of meridional temperature gradient ($\text{K}/^\circ$). (b) DJF gradient ratio $\partial_\phi \chi_{40-50} / \partial_\phi T$ versus $d\chi_{40-50} / dT$, binned by their absolute value of meridional temperature gradient ($\text{K}/^\circ$). (c) JJA gradient ratio $\partial_\phi \chi_{40-50} / \partial_\phi Q$ versus $d\chi_{40-50} / dQ$, binned by their absolute value of meridional specific humidity gradient ($\text{g}/\text{kg}/^\circ$). (d) JJA gradient ratio $\partial_\phi \chi_{20-30} / \partial_\phi \chi_{40-50}$ versus $d\chi_{20-30} / d\chi_{40-50}$, binned by their absolute value of meridional gradient of $\partial_\phi \chi_{40-50}$ ($\text{ppm}/^\circ$). Dashed line shows the 1:1 slope. RMSE between gradient ratio and regression for each bin is indicated.

202 previous studies have found robust relationships between O_3 and Q (e.g., Camalier et
 203 al., 2007; Kavassalis & Murphy, 2017; Tawfik & Steiner, 2013). To test this idea, we mod-
 204 ify (1) to explore the connection between $d\chi/dQ$ and gradient ratio of specific humid-
 205 ity $\partial_\phi \chi / \partial_\phi Q$. As shown in Figure 2c, the agreement between regression $d\chi_{40-50} / dQ$ and
 206 $\partial_\phi \chi_{40-50} / \partial_\phi Q$ is similar to that for the $\chi - T$ relationships. The more visible scatter
 207 in Figure 2c is partly due to a more complex spatial pattern of Q in the summer, where
 208 specific humidity changes non-monotonically with latitudes on land (discussed further
 209 in Section 4).

Another potential application is to use the gradient ratio to explain the regression slope between two chemical tracers, i.e. the relationship between different pollutants with different regional distribution. For example, we can regress the daily concentration of tracers emitted in the subtropics χ_{20-30} onto χ_{40-50} . Figure 2d shows $d\chi_{20-30}/d\chi_{40-50}$ against their gradient ratios $\partial_\phi\chi_{20-30}/\partial_\phi\chi_{40-50}$, scattered around the 1:1 line. Both χ_{40-50} and χ_{20-30} are negatively correlated at 20–50°N, but positively correlated outside of 20–50°N. This pattern occurs because $\partial_\phi\chi_{40-50}$ and $\partial_\phi\chi_{20-30}$ have opposite signs and therefore a negative gradient ratio between the emission regions of the two tracers (20–50°N). Similar to $d\chi/dT$, the RMSE for $\partial_\phi\chi_{20-30}/\partial_\phi\chi_{40-50}$ is the smallest when gradients are strongest ($\partial_\phi\chi_{40-50} > 0.03$ ppm/°, circles). The same applies to χ_{40-50} and χ_{60-70} , where the two tracers are negatively correlated at 40–70°N (not shown). This result suggests our framework can help explain the relationship between different pollutants based on their mean meridional gradients. For example, PM_{2.5} and O₃ have different mean meridional gradients in the southeastern US due to their different spatial distributions (e.g., Schnell & Prather, 2017).

Finally, we examine how well the gradient ratio approximates $d\chi/dT$ during summer (JJA) for tracers with different loss rates. Additional simulations have been performed of tracers with emissions between 40–50°N and loss rates $\tau = 5, 25, 100,$ and 150 days⁻¹ (Figure S1). Analysis of these simulations shows very little sensitivity to loss rates: for all tracers the gradient ratio performs best when the temperature gradient is the strongest ($|\partial_\phi T| > 0.6$ K/°) and performs poorly at weak temperature gradients ($|\partial_\phi T| < 0.2$ K/°). There is a weak sensitivity in RMSE where smaller RMSEs are found at faster loss rates (Figure S1a). This result is consistent with smaller magnitudes of $d\chi/dT$ for a tracer with a shorter lifetime, so that the absolute errors are smaller.

4 Ozone

We now consider the O₃- T relationship, and whether gradient ratio can also be used to estimate dO_3/dT . The idealized tracer experiments in the previous section illustrated equation (1) in a theoretical context. In this section, we show that these relationships also hold for a tracer (i.e., O₃) with more complex chemistry and with precursors that have spatially variable emissions. As shown in Kerr et al. (2020), there are large spatial variations in the JJA daily correlations between O₃ and T from the GMI simulation, where dO_3/dT is positive over midlatitude land north of $\sim 35^\circ\text{N}$, but negative over the oceans

(Figure 3a). The magnitude of dO_3/dT over midlatitude land varies, with regions of high values in the northeastern and Midwest US, Continental Europe, and northeastern China. At lower latitudes the sign of dO_3/dT over land varies, with positive values over central America and northern India, and negative values over northern Africa and southwestern China. A very similar pattern to Figure 3a is found for the GMI “transport-only” simulations from Kerr et al. (2020), indicating (as discussed in Kerr et al. (2020)) that the pattern of dO_3/dT is primarily a result of atmospheric transport, as opposed to atmospheric chemistry. A similar pattern for the O_3 - T relationship is also found in other chemical models (e.g., Meehl et al., 2018; Porter & Heald, 2019; Nolte et al., 2021).

Next, we examine whether these spatial variations in dO_3/dT can be explained by the gradient ratio $\partial_\phi O_3/\partial_\phi T$ (equation (2)). To do so, we compare the spatial pattern of JJA meridional gradients of ozone $\partial_\phi O_3$ and temperature $\partial_\phi T$ in Figure 3b. Ozone concentrations are highest over midlatitude land, resulting in negative $\partial_\phi O_3$ north of 40°N and positive $\partial_\phi O_3$ south of 40°N over North America (Figure 3b contours). Over Eurasia, the change of sign of $\partial_\phi O_3$ occurs at about 35°N . Combined with the negative $\partial_\phi T$ (Figure 3b shading), we expect the $\partial_\phi O_3$ pattern to yield positive dO_3/dT north of 35°N according to (2). This is indeed the case, as mentioned above; the only land regions with negative dO_3/dT are northern Africa and southwestern China. These are regions where $\partial_\phi O_3$ and $\partial_\phi T$ are positive, so the sign of dO_3/dT is again consistent with $\partial_\phi O_3/\partial_\phi T$.

The gradient ratio can also explain the prominent land-sea contrast in the dO_3/dT pattern. The offshore transport of ozone from the east coasts of North America and Asia leads to strong positive $\partial_\phi O_3$ on the western ocean basins. This pattern combines with a weak (negative) $\partial_\phi T$ over ocean to result in negative dO_3/dT . Again the sign of dO_3/dT can also be explained by (2).

To quantify the approximation of (2), we again compare the average regression and gradient ratios over 10° latitude \times 20° longitude domains (Figure 3c). Similar to idealized tracers, gradient ratios $\partial_\phi O_3/\partial_\phi T$ best estimate dO_3/dT when temperature gradients are strong ($|\partial_\phi T| > 0.6 \text{ K}/^\circ$). Although the RMSE doubles for moderate temperature gradients ($0.2 < |\partial_\phi T| < 0.6 \text{ K}/^\circ$), gradient ratio still explains 50% of the dO_3/dT variance. When temperature gradients are weak ($|\partial_\phi T| < 0.2 \text{ K}/^\circ$), gradient ratio is not a good predictor of dO_3/dT , though the signs of the two quantities agree more often than not. The same applies to the transport-only simulation (Figure 3c open sym-

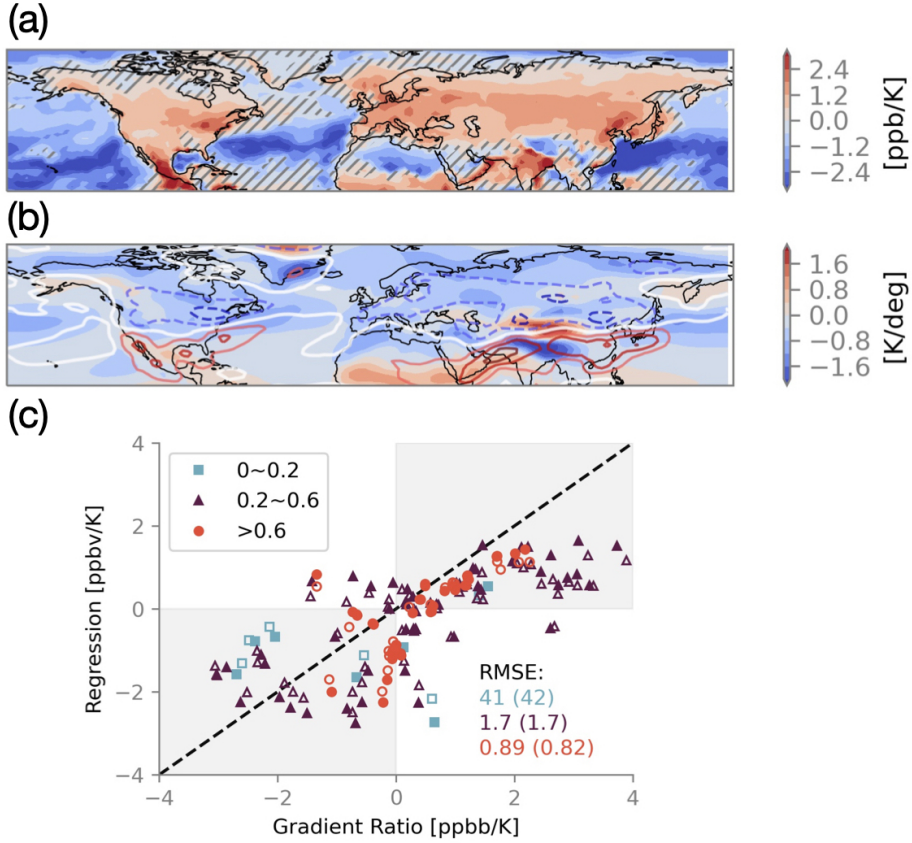


Figure 3. 2008–2010 JJA O_3 - T relationship from GMI simulation. (a) Daily dO_3/dT regression slope. Regions with $p > 0.05$ (not statistically significant) are hatched. (b) Mean meridional gradients of $\partial_\phi O_3$ in contours and of $\partial_\phi T$ in shading. Solid contours show positive $\partial_\phi O_3$ and dashed contours show negative $\partial_\phi O_3$, with an interval of 1.0 ppbv/°. (c) Gradient ratio $\partial_\phi O_3/\partial_\phi T$ versus regression dO_3/dT averaged over 10° latitude \times 20° longitude regions, binned by the absolute values of meridional temperature gradient $|\partial_\phi T|$ (K/°). Dashed line shows the 1:1 slope. RMSE between gradient ratio and regression for each bin is indicated. Open symbols and RMSE in brackets are from the transport-only simulation.

274 bols), where we see only slight shifts in dO_3/dT and $\partial_\phi O_3/\partial_\phi T$ and minor differences
 275 in RMSE from the control simulation. This result emphasizes the major role of trans-
 276 port and suggests a minor role in chemistry to shape the O_3 - T relationship.

277 There is noticeably more scattering from the 1:1 line for dO_3/dT in Figure 3c than
 278 for $d\chi_{40-50}/dT$ in Figure 1c. This difference is not surprising, given that the spatial pat-
 279 tern of O_3 is complex and zonally asymmetric, while χ_{40-50} emissions are zonally uni-

280 form. We find that the mismatch between dO_3/dT and $\partial_\phi O_3/\partial_\phi T$ is largest near promi-
 281 nent topography (e.g., the Tibetan Plateau) and over oceans away from O_3 sources (e.g.,
 282 central Pacific). Overall, $\partial_\phi O_3/\partial_\phi T$ tends to overestimate the magnitude of dO_3/dT .

283 Similar to what we find earlier with idealized tracers, the gradient ratio allows us
 284 to explain not only the O_3 - T relationship, but also other meteorological dependencies
 285 such as JJA dO_3/dQ . The midlatitude land regions have overwhelmingly positive dO_3/dQ ,
 286 while significant negative dO_3/dQ relationships are found in subtropics and most ocean
 287 basins (Figure S2a). Southeastern US and China are regions that have either positive
 288 or not significant dO_3/dT but significant dO_3/dQ . Figure S2b shading shows the spe-
 289 cific humidity meridional gradient $\partial_\phi Q$, characterized by negative values over many land
 290 regions and positive values in central Eurasia, northern Africa, and northwestern North
 291 America. Unlike T , Q maximizes locally at midlatitude continental interiors in the sum-
 292 mer, leading to a switch in sign of $\partial_\phi Q$. A quantitative comparison between regional $\partial_\phi O_3/\partial_\phi Q$
 293 and dO_3/dQ is shown on Figure S2c, binned by their magnitude of meridional specific
 294 humidity gradient $|\partial_\phi Q|$. In both the control and transport-only simulations, the gra-
 295 dient ratio $\partial_\phi O_3/\partial_\phi Q$ can capture dO_3/dQ well with the smallest RMSE in regions with
 296 moderate to strong specific humidity gradients ($|\partial_\phi Q| > 0.1$ g/kg/°). The approxima-
 297 tion produces large RMSE when specific humidity gradients are weak ($|\partial_\phi Q| < 0.1$ g/kg/°).

298 5 Discussion and Possible Implications

299 As discussed in the Introduction, it is unclear how dO_3/dT will change with cli-
 300 mate. The result that the gradient ratio can be used to approximate dO_3/dT may pro-
 301 vide some useful insight into changes with climate in regions with strong meridional tem-
 302 perature gradients. A robust result of climate projections is polar amplification (Arc-
 303 tic warms more rapidly than lower latitudes), and we expect (on average) that $|\partial_\phi T|$ in
 304 mid-latitudes will decrease with increased GHG emissions (Tamarin-Brodsky et al., 2020).
 305 This pattern would then result in an increase in the gradient ratio (and dO_3/dT) if there
 306 is no change in O_3 . However, another robust climate projection is the poleward move-
 307 ment of mid-latitude jet streams. If there is no change in O_3 precursor emissions, the
 308 projected northward jet shift in North America will result in $|\partial_\phi O_3|$ increasing north of
 309 the jet (Barnes & Fiore, 2013). An increase in $|\partial_\phi O_3|$ north of the jet and a decrease in
 310 $|\partial_\phi T|$ will both contribute to an increase in the gradient ratio (and dO_3/dT).

311 Note that Barnes and Fiore (2013) simulation with increasing GHG emissions but
 312 constant O₃ precursor emissions show an increase in dO_3/dT north of the jet but decrease
 313 south of the jet (see arrows in Figure 3j of Barnes and Fiore (2013)), which is partly con-
 314 sistent with the above arguments on changes in meridional gradients. More detailed anal-
 315 ysis of climate projections is needed to determine exactly how the O₃ and temperature
 316 gradients as well as dO_3/dT change, and if the changes in gradient ratio explains the change
 317 in dO_3/dT . However, our preliminary consideration of expected polar amplification and
 318 changes in the jet streams indicates that dO_3/dT will likely change, and caution should
 319 be used if predicting the impact of climate warming on O₃ from observed dO_3/dT .

320 6 Conclusion

321 Although the temporal correlation between O₃ and T is often explained in terms
 322 of the temperature dependence of chemical reactions or emissions, we show here that the
 323 dO_3/dT regression is primarily an indirect association due to the meridional advection
 324 of both O₃ and T . Further we show that dO_3/dT can be estimated by the ratio of the
 325 time-mean O₃ and T meridional gradients (the “gradient ratio”): variations in the gra-
 326 dient ratio explain the opposite signs in dO_3/dT between midlatitude land and ocean,
 327 as well as the differences in sign among subtropical land regions. The quantitative ac-
 328 curacy of this approximation (equation (1)) depends on the magnitude of the meridional
 329 temperature gradient $|\partial_\phi T|$: it works well when $|\partial_\phi T|$ is strong, but not in regions of weak
 330 $|\partial_\phi T|$.

331 The agreement between the gradient ratio and dO_3/dT provides an approach to
 332 understand how dO_3/dT may change with climate. Our preliminary consideration of ex-
 333 pected changes meridional gradients of T and O₃ due to polar amplification and jet stream
 334 shifts, respectively, indicates that dO_3/dT will likely change, suggesting caution is re-
 335 quired if using the present-day dO_3/dT to estimate the impact of climate on O₃. How-
 336 ever, further analysis is needed to quantify exactly how meridional gradients and dO_3/dT
 337 may change with climate.

338 The key role of meridional advection, and the agreement between the regression
 339 and gradient ratio is a general result. It holds for O₃ with Q , and also for the relation-
 340 ship of idealized tracers (with lifetimes between 5 and 150 days) with T or Q , or between
 341 idealized tracers with different source regions. This result suggests that consideration

342 of meridional gradients may provide insights in the relationship between PM_{2.5} and me-
343 teorology, as well as the co-occurrence of O₃ and PM_{2.5} pollution events. Future work
344 is planned to explore this possibility.

345 Acknowledgments

346 We thank Arlene Fiore, Jean-Francois Lamarque, and Sarah Strode for helpful com-
347 ments and discussions. This work was funded by support from the US National Science
348 Foundation and the National Aeronautics and Space Administration (NASA).

349 Data Availability Statement

350 GEOS-Chem simulations were run on the Maryland Advanced Research Comput-
351 ing Center (MARCC). GEOS-Chem idealized tracer simulation data are available at [https://](https://doi.org/10.6084/m9.figshare.16989856.v1)
352 doi.org/10.6084/m9.figshare.16989856.v1. NASA GMI CTM output is publicly avail-
353 able on the data portal for the NASA Center for Climate Simulation ([portal.nccs.nasa](https://portal.nccs.nasa.gov/datashare/dirac)
354 [.gov/datashare/dirac](https://portal.nccs.nasa.gov/datashare/dirac)). NASA's Global Modeling and Assimilation Office and God-
355 dard Earth Sciences Data and Information Services Center (GES DISC) provided and
356 disseminated the MERRA-2 data used in this study, specifically the *inst3_3d_asm_Np* col-
357 lection (Global Modeling And Assimilation Office (GMAO), 2015).

358 References

- 359 Barnes, E. A., & Fiore, A. M. (2013). Surface ozone variability and the jet
360 position: Implications for projecting future air quality. *Geophysical Re-*
361 *search Letters*, *40*(11), 2839–2844. Retrieved 2021-03-01, from [https://](https://agupubs.onlinelibrary.wiley.com/doi/abs/10.1002/grl.50411)
362 agupubs.onlinelibrary.wiley.com/doi/abs/10.1002/grl.50411 doi:
363 <https://doi.org/10.1002/grl.50411>
- 364 Bloomer, B. J., Stehr, J. W., Piety, C. A., Salawitch, R. J., & Dickerson, R. R.
365 (2009). Observed relationships of ozone air pollution with temperature
366 and emissions. *Geophysical Research Letters*, *36*(9). Retrieved 2021-04-
367 23, from [https://agupubs.onlinelibrary.wiley.com/doi/abs/10.1029/](https://agupubs.onlinelibrary.wiley.com/doi/abs/10.1029/2009GL037308)
368 [2009GL037308](https://agupubs.onlinelibrary.wiley.com/doi/abs/10.1029/2009GL037308) doi: <https://doi.org/10.1029/2009GL037308>
- 369 Camalier, L., Cox, W., & Dolwick, P. (2007). The effects of meteorology on
370 ozone in urban areas and their use in assessing ozone trends. *Atmospheric*
371 *Environment*, *41*(33), 7127–7137. Retrieved 2021-10-18, from <https://>

- 372 www.sciencedirect.com/science/article/pii/S1352231007004165 doi:
373 10.1016/j.atmosenv.2007.04.061
- 374 Duncan, B. N., Strahan, S. E., Yoshida, Y., Steenrod, S. D., & Livesey, N. (2007).
375 Model study of the cross-tropopause transport of biomass burning pollution.
376 *Atmospheric Chemistry and Physics*, 7(14), 3713–3736. Retrieved 2021-07-27,
377 from <https://acp.copernicus.org/articles/7/3713/2007/> (Publisher:
378 Copernicus GmbH) doi: 10.5194/acp-7-3713-2007
- 379 Fu, T.-M., & Tian, H. (2019). Climate Change Penalty to Ozone Air Quality: Re-
380 view of Current Understandings and Knowledge Gaps. *Current Pollution Re-*
381 *ports*, 5(3), 159–171. Retrieved 2021-06-22, from [https://doi.org/10.1007/](https://doi.org/10.1007/s40726-019-00115-6)
382 [s40726-019-00115-6](https://doi.org/10.1007/s40726-019-00115-6) doi: 10.1007/s40726-019-00115-6
- 383 Global Modeling And Assimilation Office (GMAO). (2015). *MERRA-2*
384 *inst3_3d_asm_np: 3d, 3-hourly, instantaneous, pressure-level, assimilation,*
385 *assimilated meteorological fields v5.12.4.* NASA/GSFC, Greenbelt, MD, USA,
386 NASA Goddard Earth Sciences Data and Information Services Center (GES
387 DISC). Retrieved from [https://disc.gsfc.nasa.gov/datacollection/](https://disc.gsfc.nasa.gov/datacollection/M2I3NPASM_5.12.4.html)
388 [M2I3NPASM_5.12.4.html](https://disc.gsfc.nasa.gov/datacollection/M2I3NPASM_5.12.4.html) (NASA/GSFC, Greenbelt, MD, USA, NASA God-
389 dard Earth Sciences Data and Information Services Center (GES DISC).
390 Accessed 07/19/2021) doi: 10.5067/QBZ6MG944HW0
- 391 Kavassalis, S. C., & Murphy, J. G. (2017). Understanding ozone-meteorology cor-
392 relations: A role for dry deposition. *Geophysical Research Letters*, 44(6),
393 2922–2931. Retrieved 2021-07-21, from [https://agupubs.onlinelibrary](https://agupubs.onlinelibrary.wiley.com/doi/abs/10.1002/2016GL071791)
394 [.wiley.com/doi/abs/10.1002/2016GL071791](https://agupubs.onlinelibrary.wiley.com/doi/abs/10.1002/2016GL071791) doi: 10.1002/2016GL071791
- 395 Kerr, G. H., & Waugh, D. W. (2018). Connections between summer air pollution
396 and stagnation. *Environmental Research Letters*, 13(8), 084001. Retrieved
397 2021-06-27, from <https://doi.org/10.1088/1748-9326/aad2e2> (Publisher:
398 IOP Publishing) doi: 10.1088/1748-9326/aad2e2
- 399 Kerr, G. H., Waugh, D. W., & Miller, S. M. (2021). Jet Stream-Surface Tracer Rela-
400 tionships: Mechanism and Sensitivity to Source Region. *Geophysical Research*
401 *Letters*, 48(1), e2020GL090714. Retrieved 2021-02-24, from [https://agupubs](https://agupubs.onlinelibrary.wiley.com/doi/abs/10.1029/2020GL090714)
402 [.onlinelibrary.wiley.com/doi/abs/10.1029/2020GL090714](https://agupubs.onlinelibrary.wiley.com/doi/abs/10.1029/2020GL090714) doi: [https://](https://doi.org/10.1029/2020GL090714)
403 doi.org/10.1029/2020GL090714
- 404 Kerr, G. H., Waugh, D. W., Steenrod, S. D., Strode, S. A., & Strahan, S. E.

- 405 (2020). Surface Ozone-Meteorology Relationships: Spatial Variations
406 and the Role of the Jet Stream. *Journal of Geophysical Research: Atmo-*
407 *spheres*, 125(21), e2020JD032735. Retrieved 2021-02-24, from [https://](https://agupubs.onlinelibrary.wiley.com/doi/abs/10.1029/2020JD032735)
408 agupubs.onlinelibrary.wiley.com/doi/abs/10.1029/2020JD032735 doi:
409 <https://doi.org/10.1029/2020JD032735>
- 410 Kerr, G. H., Waugh, D. W., Strode, S. A., Steenrod, S. D., Oman, L. D., & Stra-
411 han, S. E. (2019). Disentangling the Drivers of the Summertime Ozone-
412 Temperature Relationship Over the United States. *Journal of Geophys-*
413 *ical Research: Atmospheres*, 124(19), 10503–10524. Retrieved 2021-06-27,
414 from [https://agupubs.onlinelibrary.wiley.com/doi/abs/10.1029/](https://agupubs.onlinelibrary.wiley.com/doi/abs/10.1029/2019JD030572)
415 [2019JD030572](https://doi.org/10.1029/2019JD030572) doi: 10.1029/2019JD030572
- 416 Landrigan, P. J., Fuller, R., Acosta, N. J. R., Adeyi, O., Arnold, R., Basu,
417 N. N., ... Boufford, J. I. e. a. (2018). The Lancet Commission on pol-
418 lution and health. *The Lancet*, 391(10119), 462–512. Retrieved 2021-
419 08-09, from [https://www.thelancet.com/journals/lancet/article/](https://www.thelancet.com/journals/lancet/article/PIIS0140-6736(17)32345-0/abstract)
420 [PIIS0140-6736\(17\)32345-0/abstract](https://doi.org/10.1016/S0140-6736(17)32345-0) (Publisher: Elsevier) doi:
421 [10.1016/S0140-6736\(17\)32345-0](https://doi.org/10.1016/S0140-6736(17)32345-0)
- 422 Meehl, G. A., Tebaldi, C., Tilmes, S., Lamarque, J.-F., Bates, S., Pendergrass,
423 A., & Lombardozi, D. (2018). Future heat waves and surface ozone. *En-*
424 *vironmental Research Letters*, 13(6), 064004. Retrieved 2021-03-15, from
425 <https://doi.org/10.1088/1748-9326/aabcdc> (Publisher: IOP Publishing)
426 doi: 10.1088/1748-9326/aabcdc
- 427 Nolte, C. G., Spero, T. L., Bowden, J. H., Sarofim, M. C., Martinich, J., & Mallard,
428 M. S. (2021). Regional Temperature-Ozone Relationships Across the U.S.
429 Under Multiple Climate and Emissions Scenarios. *Journal of the Air & Waste*
430 *Management Association*. Retrieved 2021-09-10, from [https://doi.org/](https://doi.org/10.1080/10962247.2021.1970048)
431 [10.1080/10962247.2021.1970048](https://doi.org/10.1080/10962247.2021.1970048) doi: 10.1080/10962247.2021.1970048
- 432 Porter, W. C., & Heald, C. L. (2019). The mechanisms and meteorological
433 drivers of the summertime ozone-temperature relationship. *Atmospheric*
434 *Chemistry and Physics*, 19(21), 13367–13381. Retrieved 2021-07-28, from
435 <https://acp.copernicus.org/articles/19/13367/2019/> (Publisher:
436 Copernicus GmbH) doi: 10.5194/acp-19-13367-2019
- 437 Rasmussen, D. J., Hu, J., Mahmud, A., & Kleeman, M. J. (2013). The

- 438 Ozone–Climate Penalty: Past, Present, and Future. *Environmental Sci-*
439 *ence & Technology*, 47(24), 14258–14266. Retrieved 2021-05-10, from
440 <https://doi.org/10.1021/es403446m> (Publisher: American Chemical
441 Society) doi: 10.1021/es403446m
- 442 Schnell, J. L., & Prather, M. J. (2017). Co-occurrence of extremes in surface
443 ozone, particulate matter, and temperature over eastern North America.
444 *Proceedings of the National Academy of Sciences*, 114(11), 2854–2859. Re-
445 trieved 2021-08-09, from <https://www.pnas.org/content/114/11/2854>
446 (Publisher: National Academy of Sciences Section: Physical Sciences) doi:
447 10.1073/pnas.1614453114
- 448 Shen, L., Mickley, L. J., & Murray, L. T. (2017). Influence of 2000–2050 climate
449 change on particulate matter in the United States: results from a new statisti-
450 cal model. *Atmospheric Chemistry and Physics*, 17(6), 4355–4367. Retrieved
451 2021-09-15, from <https://acp.copernicus.org/articles/17/4355/2017/>
452 (Publisher: Copernicus GmbH) doi: 10.5194/acp-17-4355-2017
- 453 Strahan, S. E., Douglass, A. R., & Newman, P. A. (2013). The contributions of
454 chemistry and transport to low arctic ozone in March 2011 derived from Aura
455 MLS observations. *Journal of Geophysical Research: Atmospheres*, 118(3),
456 1563–1576. Retrieved 2021-07-27, from [https://agupubs.onlinelibrary](https://agupubs.onlinelibrary.wiley.com/doi/abs/10.1002/jgrd.50181)
457 [.wiley.com/doi/abs/10.1002/jgrd.50181](https://agupubs.onlinelibrary.wiley.com/doi/abs/10.1002/jgrd.50181) doi: 10.1002/jgrd.50181
- 458 Strahan, S. E., Duncan, B. N., & Hoor, P. (2007). Observationally derived
459 transport diagnostics for the lowermost stratosphere and their applica-
460 tion to the GMI chemistry and transport model. *Atmospheric Chem-*
461 *istry and Physics*, 7(9), 2435–2445. Retrieved 2021-07-27, from [https://](https://acp.copernicus.org/articles/7/2435/2007/)
462 acp.copernicus.org/articles/7/2435/2007/ (Publisher: Copernicus
463 GmbH) doi: 10.5194/acp-7-2435-2007
- 464 Strode, S. A., Rodriguez, J. M., Logan, J. A., Cooper, O. R., Witte, J. C., Lamsal,
465 L. N., ... Strahan, S. E. (2015). Trends and variability in surface ozone over
466 the United States. *Journal of Geophysical Research: Atmospheres*, 120(17),
467 9020–9042. Retrieved 2021-09-17, from [https://onlinelibrary.wiley.com/](https://onlinelibrary.wiley.com/doi/abs/10.1002/2014JD022784)
468 [doi/abs/10.1002/2014JD022784](https://onlinelibrary.wiley.com/doi/abs/10.1002/2014JD022784) doi: 10.1002/2014JD022784
- 469 Tai, A. P. K., & Val Martin, M. (2017). Impacts of ozone air pollution and temper-
470 ature extremes on crop yields: Spatial variability, adaptation and implications

- 471 for future food security. *Atmospheric Environment*, 169, 11–21. Retrieved
472 2021-08-09, from [https://www.sciencedirect.com/science/article/pii/
473 S1352231017305836](https://www.sciencedirect.com/science/article/pii/S1352231017305836) doi: 10.1016/j.atmosenv.2017.09.002
- 474 Tamarin-Brodsky, T., Hodges, K., Hoskins, B. J., & Shepherd, T. G. (2020).
475 Changes in Northern Hemisphere temperature variability shaped by regional
476 warming patterns. *Nature Geoscience*, 13(6), 414–421. Retrieved 2021-04-29,
477 from <https://www.nature.com/articles/s41561-020-0576-3> (Number: 6
478 Publisher: Nature Publishing Group) doi: 10.1038/s41561-020-0576-3
- 479 Tawfik, A. B., & Steiner, A. L. (2013). A proposed physical mechanism for ozone-
480 meteorology correlations using land-atmosphere coupling regimes. *Atmo-
481 spheric Environment*, 72, 50–59. Retrieved 2021-10-18, from [https://
482 www.sciencedirect.com/science/article/pii/S1352231013001672](https://www.sciencedirect.com/science/article/pii/S1352231013001672) doi:
483 10.1016/j.atmosenv.2013.03.002
- 484 Westervelt, D. M., Horowitz, L. W., Naik, V., Tai, A. P. K., Fiore, A. M., &
485 Mauzerall, D. L. (2016). Quantifying PM_{2.5}-meteorology sensitivities in
486 a global climate model. *Atmospheric Environment*, 142, 43–56. Retrieved
487 2021-09-15, from [https://www.sciencedirect.com/science/article/pii/
488 S135223101630560X](https://www.sciencedirect.com/science/article/pii/S135223101630560X) doi: 10.1016/j.atmosenv.2016.07.040
- 489 Wittig, V. E., Ainsworth, E. A., & Long, S. P. (2007). To what extent do cur-
490 rent and projected increases in surface ozone affect photosynthesis and stom-
491 atal conductance of trees? A meta-analytic review of the last 3 decades of
492 experiments. *Plant, Cell & Environment*, 30(9), 1150–1162. Retrieved
493 2021-08-09, from [https://onlinelibrary.wiley.com/doi/abs/10.1111/
494 j.1365-3040.2007.01717.x](https://onlinelibrary.wiley.com/doi/abs/10.1111/j.1365-3040.2007.01717.x) doi: 10.1111/j.1365-3040.2007.01717.x
- 495 Wu, S., Mickley, L. J., Leibensperger, E. M., Jacob, D. J., Rind, D., & Streets,
496 D. G. (2008). Effects of 2000–2050 global change on ozone air quality in the
497 United States. *Journal of Geophysical Research: Atmospheres*, 113(D6). Re-
498 trieved 2021-05-08, from [https://agupubs.onlinelibrary.wiley.com/doi/
499 abs/10.1029/2007JD008917](https://agupubs.onlinelibrary.wiley.com/doi/abs/10.1029/2007JD008917) doi: <https://doi.org/10.1029/2007JD008917>